

# Superbubbles as the source of dynamical friction: gas migration, stellar and dark matter contributions

Rain Kipper<sup>1\*</sup>, Indrek Vurm<sup>1</sup>, Aikaterini Niovi Triantafyllaki<sup>1</sup>, Peeter Tenjes<sup>1</sup>, and Elmo Tempel<sup>1,2</sup>

<sup>1</sup> Tartu Observatory, University of Tartu, Observatooriumi 1, Tõravere 61602, Estonia

<sup>2</sup> Estonian Academy of Sciences, Kohtu 6, 10130 Tallinn, Estonia

Received X / Accepted X

## ABSTRACT

The gas distribution in galaxies is smooth on large scales but is usually inhomogeneous as well as time-dependent on smaller scales. The time-dependence originates from processes such as cloud formation, their collisions and supernovae (SNe) explosions. The inhomogeneities in the matter distribution give rise to variations in the local galactic gravitational potential, which can contribute towards dynamically coupling the gas disk to the stellar and the dark matter (DM) components of the galaxy. Specifically, multiple supernovae occurring in young stellar clusters give rise to superbubbles (SB), which modify the local acceleration field and alter the energy and momentum of stars or DM particles traversing them, in broad analogy to the dynamical friction caused by a massive object. We aim to quantify how the acceleration field from SBs causes dynamical friction and contributes to the secular evolution of galaxies. In order to assess this, we construct the density modifications to the gas distribution that mimics a SB. By evaluating the acceleration field from these density modifications, we see how the momentum or angular momentum of the gas hosting the SBs changes when stars pass through the SB. Combining the effects of all the stars and SBs we, construct an empirical approximation formula for the momentum loss in homogeneous and isotropic cases. We find that the rate at which the gas disc loses its specific angular momentum via the above process is up to 4% per Gyr, which translates to under half of its original value over the lifetime of the disc. Finally, we studied how the dynamical coupling of the gas disk with the DM halo depends on assumptions on the halo kinematics (e.g. rotation) and found a  $\sim 0.3\%$  variation in the gas disc secular evolution between different DM kinematic models.

**Key words.** galaxies: kinematics and dynamics – methods: miscellaneous – cosmology: dark matter

## 1. Introduction

In this paper we aim to study two aspects of galaxy structure, gas inhomogeneities that cause dynamical friction in gaseous discs of galaxies and corresponding secular evolution of these gas discs. Specifically, in this paper we focus on superbubbles (SB) in gas discs created by supernovae (SN) explosions as the source of dynamical friction.

SBs are cavities in the gas distribution and they span from a hundred parsecs to kiloparsecs. Nath et al. (2020) compared the size distributions of observed HI holes from *THINGS* (Walter et al. 2008) with those derived from detailed hydrodynamical simulations and concluded that SBs are caused by multiple supernovae (SNe) in a large OB association or in multiple associations. Many observations document the phenomenon as dark regions in the gas disks of galaxies such as Lara-López et al. (2023). Recent studies using JWST observations give excellent samples of SBs in NGC 628 (Watkins et al. 2023). In addition, studies like Brinks et al. (2007); Walter et al. (2008) provide good observations of holes in HI distribution in NGC 6946 by (see Fig. 1). The association of HI holes and SN explosions were studied in detail by, e.g. Lara-López et al. (2023); Sarbadhicary et al. (2023); Barnes et al. (2023).

From a physical perspective, superbubbles are under-dense regions within the gaseous medium filled by hot pressurized gas, created by multiple SN explosions that inflate a cavity within the ambient medium, driving a shock wave into the latter and accu-

mulating gas at its edges (Mac Low & McCray 1988). When the SN energy input ceases, the SB starts to dissolve. The hot interior exchanges the heat with edges via thermal conduction (Yadav et al. 2017) (hereafter Y17), causing heat to diffuse towards the cold shell and the shell material to evaporate towards the interior of the bubble (Cowie & McKee 1977). During both phases, the shell of the SB is either expanding or shrinking, causing disturbances in density and gravitational potential. An overview of these processes is provided by Keller (2017). Physically, the situation is rather complex, as the heat conduction may depend on magnetic fields, and the initial gas distribution may be clumpy instead of being homogeneous. These aspects may be relevant and were studied in Keller et al. (2014).

We aim to expand the studies of SBs and their gravitational interaction with the galaxy disc, as the current status of this research is not extensive. García-Conde et al. (2023), while not aiming to solve the SBs influence to the structure of galaxies, notes that in low density environments, and connecting them to bending waves, SNe, can redistribute gas and cause acceleration field changes. In the context of dwarf and high redshift clumpy galaxies, the strong scattering of giant clouds and holes may help to form exponential-like discs (Struck & Elmegreen 2017; Wu et al. 2020). However, these works concentrated on turbulent rather than quiet disc galaxies.

As a rule, the gas disc and the stellar disc of galaxies rotate with somewhat different velocities – the stellar disc has a slower rotation. Therefore there is, on average, a systematic mismatch between the velocities of the stars and the SBs, which can give rise to a net momentum/energy transfer between the stars

\* E-mail: rain.kipper@ut.ee

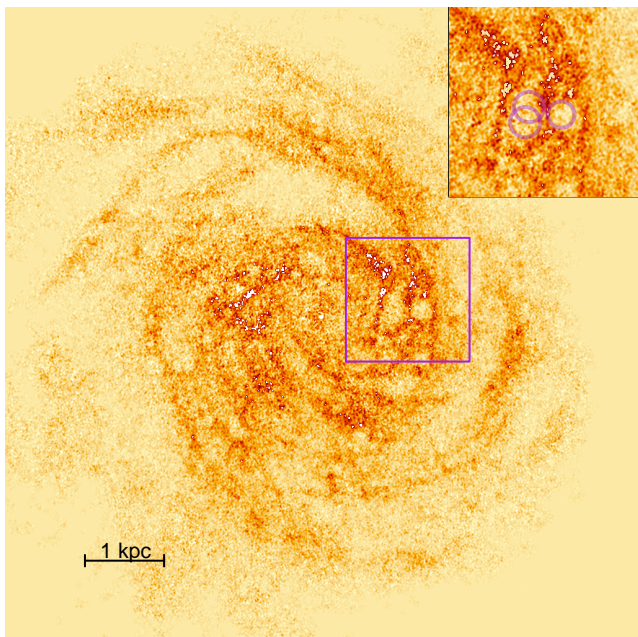


**Fig. 1.** An illustration of superbubbles (SBs) in galaxy NGC 6946 from the intensity map of THINGS survey (Walter et al. 2008). The top-right panel is a zoomed window of a fraction of galaxy where the locations of three SBs are provided (pink circles). A more detailed map of all the bubbles in the galaxy is shown in Brinks et al. (2007).

traversing the SB and the gaseous environment. In case of a massive perturber in a stellar environment this is called dynamical friction (Chandrasekhar 1943). In Kipper et al. (2020, 2023) we developed a method to calculate dynamical friction effects in a non-homogeneous gravitational potential. In present paper, we use the method for the case of SBs. For this we need to know the (positive or negative) density contrast of a SB, relative to the host environment.

Dynamical friction acts in two ways: it changes both the velocities of stars and the velocities of SBs, causing the evolution of the disc. These changes are slow (secular). There are various other processes causing the secular evolution of galaxies (Kuzmin 1961, 1963; Binney 2013; Kipper et al. 2021; Huško et al. 2023), also see a review by Kormendy (2013). Getting a grasp on these processes is necessary to reach the understanding level to reproduce all galaxy aspects in simulations. A good understanding of the baryonic effects also allows to improve dark matter (DM) studies (Maxwell et al. 2015). The list of internal processes that contribute to secular evolution include scattering of stars (characterized by the Fokker-Planck equation, see Binney & Tremaine (2008)), churning (the change of angular momentum by spiral, bar or other non-axisymmetry) (Sellwood & Binney 2002; Minchev & Famaey 2010; Vera-Ciro et al. 2014; Patil et al. 2023), blurring (the breath of orbit grows, (Schönrich & Binney 2009) out to very high galactic radii (Lian et al. 2022)) and local disc instabilities (Huško et al. 2023). These processes provide significant redistribution of matter in galaxies. In the present paper, we study an additional effect that possibly causes a slow redistribution of stars and gas. Similarly to giant molecular clouds acting as scatterers of stars, we investigate how much SBs alter the gas distribution.

The purpose of the current paper is to investigate, whether the time-dependent gravitational potential disturbances help to transfer angular momentum between the gas disc and stellar disc in a smooth and relatively unperturbed (regular) galaxy. And

thereafter, are the contributions sufficient to cause significant migration of gas disc?

In Sect. 2 we characterise our description of the SB and its evolution, Sect. 3 we show how passing the SB influences the single star kinematics numerically and provide analytical approximations for it; Sect. 4 shows numerically the transfer of momentum or angular momentum in various environments. We discuss the results in Sect. 5 and summarise in 6.

## 2. Description of a superbubble (SB)

SBs are, in essence, underdense regions embedded within some background gaseous environment (host). In our present treatment, we consider this background to be homogeneous and describe the SB as a spherical region with (formally) negative interior density relative to the background, surrounded by a slightly overdense shell of material displaced from the interior. We will subsequently consider the effect of such configuration on the local acceleration field relative that of the unperturbed host.

### 2.1. The density profile

At any moment of time we approximate the SB density profile using two parameters: its inner and outer radius,  $R_i$  and  $R_o$ , respectively. The inner radius is the radius closer to the center of the cavity before the overdensity region, and the outer radius is the one closer to the ISM, the edges of the SB. For convenience we also denote their midpoint  $R_m = (R_i + R_o)/2$ . The approximation of the SB aims to mimic the profile from Y17 paper, where they simulated the evolution of a SB in a homogeneous gas environment with initial density  $\rho_{\text{env}} = 0.015 M_{\odot} \text{pc}^{-3}$ . The profile itself is shown in Y17 figure A1. Our approximation assumes that the SNe have pushed out all the gas inside  $R_i$ . Hence physical density inside it is zero, but in the form of density-correction  $\rho^* \equiv \rho - \rho_{\text{env}}$  its value is  $-\rho_{\text{env}}$ . In our description, the gas from inside is pushed between  $R_i$  and  $R_o$  where we describe the density distribution as a quadratic polynomial. Outside of  $R_o$ , the SB has had no influence and the density-correction is zero. Combining all the regions together, we have the formula

$$\rho^* \equiv \rho - \rho_{\text{env}} = \begin{cases} -\rho_{\text{env}}, & R < R_i \\ B - A(R - R_m)^2, & R_i \leq R \leq R_o \\ 0, & R > R_o \end{cases} \quad (1)$$

The coefficients  $A$  and  $B$  are found from mass conservation, i.e. the mass shifted from within radius  $R_i$  equals that added between  $R_i$  and  $R_o$  and at  $\rho^*(R_i) = \rho^*(R_o) = 0$ . Figure 2 shows this profile visually.

### 2.2. The SB evolution

SBs are short-lived compared to galaxies – they vanish soon after the SNe of the star-forming region cease. We split the description of the evolution into two phases: the expanding phase, where the SNe are pushing the gas out, and the vanishing phase, where the SNe support ceases, and SB starts to shrink. We call this phase as collapsing phase to emphasize our assumption. We denote the time of the split between the phases as  $t_{\text{max}}$ .

The Y17 simulation describes only the first 30 Myr of the SB evolution as this is an approximate age when the least massive core-collapse SNe explode. Thus, we denote this as the expansion phase. We approximate the evolution of both  $R_i$  and  $R_o$  as a power law with 2 and 3 free parameters, respectively. For the vanishing

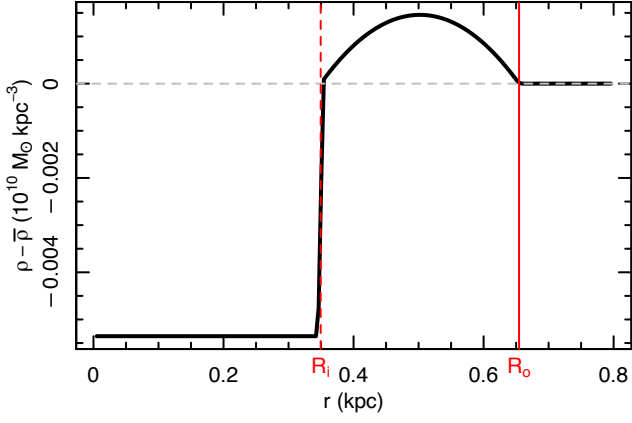


**Fig. 2.** Density contrast profile approximation of the SB at  $t = 30$  Myr inspired by the simulated SB behaviour in Y17 and described in Sect. 2.1.

of the SB phase, which was not covered by the Y17 simulation, we assume the scenario describable with a characteristic speed that we treat as constant. It mimics a collapse to occur for both  $R_i$  and  $R_o$  with a constant speed  $v_{\text{col}}$ . We denote the lifetime of the SB with  $t_{\text{end}}$  being defined as a time when the  $R_i$  shrinks back to 0 kpc. The analytical form for  $R_i$  is

$$R_i^{\text{fid}} = \begin{cases} (t/t_{i,e})^{\alpha_{i,e}}, & t \leq t_{\text{max}} \\ R_{\text{max},i} - v_{\text{col}}(t - t_{\text{max},i}) & t_{\text{max}} < t \leq t_{\text{end}} \\ 0, & t > t_{\text{end}} \end{cases} \quad (2)$$

and for  $R_o$

$$R_o^{\text{fid}} = \begin{cases} R_{o0} + (t/t_{o,s})^{\alpha_o}, & t \leq t_{\text{max}} \\ R_{\text{max},o} - v_{\text{col}}(t - t_{\text{max},i}) & t > t_{\text{max}}. \end{cases} \quad (3)$$

We approximated the parameters in this formula to match the evolution provided in the Y17 paper, and derived the following values:  $t_{i,e} = 290$  Myr,  $\alpha_{i,e} = 0.47$ ,  $R_{o0} = 60$  pc,  $t_{o,s} = 56.7$  Myr,  $\alpha_o = 0.815$ . In addition, we have denoted  $R_{\text{max},i}$  and  $R_{\text{max},o}$  as the SB inner and outer size at  $t_{\text{max}}$ ;  $v_{\text{col}}$  as the collapsing speed and superscript 'fid' denotes the fiducial run of the simulation. The evolution of  $R_i^{\text{fid}}$  and  $R_o^{\text{fid}}$  is shown in Fig. 3 as dashed and solid red lines.

Although the Y17 paper concentrates on their fiducial model, they provided some scaling relations for different SBs. In the current case, the relevant one is the scaling of the SB radii depending on the number of progenitor SNe. The scaling behaves as the modifier of radii, i.e.  $R_i$  and  $R_o$  are found from fiducial values by multiplying them with the term  $s_r$  or equivalently:

$$s_r = \frac{R_i}{R_i^{\text{fid}}} = \frac{R_o}{R_o^{\text{fid}}}. \quad (4)$$

Y17 shows that  $s_r$  depends on the number progenitor SNe as  $N_{\text{SN}}^{1/5}$ . The fiducial model corresponded to 100 SNe, hence

$$s_r = \left( \frac{N_{\text{SN}}}{100} \right)^{1/5}. \quad (5)$$

To match the number of SNe with the mass of their progenitor open clusters we use the initial mass function (IMF)  $\Psi dm$ . We match the IMF normalisation to the mass of the SB progenitor open cluster ( $M_{\text{OC}}$ ) by introducing a normalising constant  $n_{\text{IMF}}$  so that

$$\int_0^{\infty} mn_{\text{IMF}}\Psi(m)dm = M_{\text{OC}}. \quad (6)$$

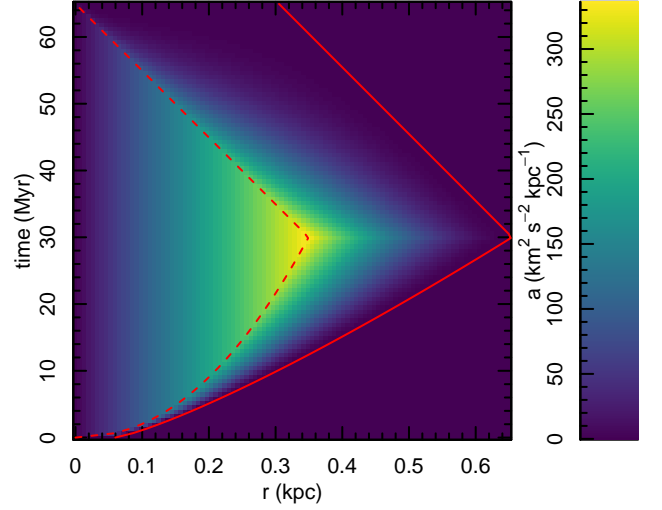


**Fig. 3.** Acceleration field of SB. Solid and dashed red line is the outer and inner radius of the fiducial model from Y17 and are described with Eqs. (8) and (9). The colorscale shows the radial acceleration values described in Sect. 3.

Secondly, we are interested in the number of stars that can produce core-collapse SNe. In terms of IMF it is an integral between the suitable mass range ( $m_{\text{SN},\text{min}} \dots m_{\text{SN},\text{max}}$ ):

$$N_{\text{SN}} = \int_{m_{\text{SN},\text{min}}}^{m_{\text{SN},\text{max}}} n_{\text{IMF}}\Psi(m) dm = M_{\text{OC}} \frac{\int_{m_{\text{SN},\text{min}}}^{m_{\text{SN},\text{max}}} \Psi(m) dm}{\int_0^{\infty} m\Psi(m) dm}. \quad (7)$$

The division of integrals provides the number of supernovae per unit cluster mass which we denote as  $\vartheta$  so that  $N_{\text{SN}} = \vartheta M_{\text{OC}}$ .

For the numerical evaluation of  $\vartheta$  we need to specify  $\Psi$ ,  $m_{\text{SN},\text{min}}$  and  $m_{\text{SN},\text{max}}$ . For the  $\Psi$  we selected the Kroupa IMF (Kroupa 2001), the  $m_{\text{SN},\text{min}} = 8 M_{\odot}$ , but the  $m_{\text{SN},\text{max}}$  is not well determined. There has been observed dimming periods of massive stars and hints of faint/absent supernovae with masses above  $m_{\text{SN},\text{max}} = 17 M_{\odot}$  Reynolds et al. (2015); Byrne & Fraser (2022) show that there is a lack of SNe with masses above  $m_{\text{SN},\text{max}} = 17 M_{\odot}$ , although it is not yet concluded. Therefore it is possible that the highest mass stars do not explode as supernovae and we should adopt  $m_{\text{SN},\text{max}} = 17 M_{\odot}$ , but it is unclear if this affects all or some fraction of massive stars. The conventional text-book value is still  $m_{\text{SN},\text{max}} = \infty M_{\odot}$  for integrations. In these cases, the values are  $\vartheta_{17} = 0.0054 M_{\odot}^{-1}$  and  $\vartheta_{\infty} = 0.0084 M_{\odot}^{-1}$ . In the current paper we adopt the more classical  $\vartheta = \vartheta_{\infty}$ .

Combining all together, we see that for the cluster mass of  $M_{\text{OC}}$  the inner and outer radii are determined from

$$R_i = R_i^{\text{fid}} (\vartheta M_{\text{OC}} / 100)^{1/5}, \quad (8)$$

$$R_o = R_o^{\text{fid}} (\vartheta M_{\text{OC}} / 100)^{1/5}. \quad (9)$$

### 2.3. Selecting open clusters able to produce SBs

The inflation of a SB is not guaranteed in all open clusters as not all them are able to produce a sufficient number of SNe for that. According to Y17, the necessary amount for SBs is  $N_{\text{SN},\text{lim}} \approx 100$ . The mass of the open cluster corresponding to it

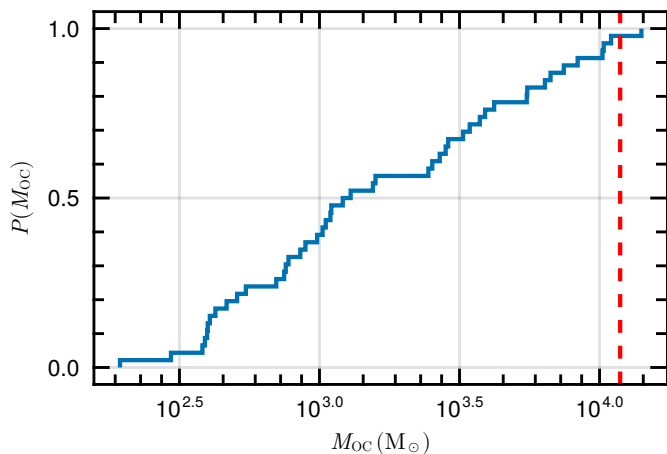


**Fig. 4.** Cumulative distribution of open cluster initial mass function from Bhattacharya et al. (2022) used to determine the open clusters able to produce SNe in Sect. 2.3. The vertical dashed line shows  $M_{\text{OC,lim}}$  defined with Eq. (10)

is

$$M_{\text{OC,lim}} \equiv N_{\text{SN,lim}}/\vartheta \approx 11\,800 M_{\odot}. \quad (10)$$

Let us turn our attention to the fraction of open clusters able to produce a SB, their average masses and the corresponding parameter  $s_r$  defined in Eq. (5). We take the open cluster initial mass function ( $\equiv \Psi_{\text{OC}}$ ) from the Milky Way (MW) observations. The MW is in a calm non-merger state that produces a basis to study the secular evolution aspects in galaxies. The data for  $\Psi_{\text{OC}}$  is taken from Bhattacharya et al. (2022) and is shown in Fig. 4.

Only one open cluster in the  $\Psi_{\text{OC}}$  is above the  $M_{\text{OC,lim}}$  indicating that very few open clusters are able to form a stable SB. The mass of the cluster is  $14\,108 M_{\odot}$ , providing the effective value as

$$s_r = 1.19. \quad (11)$$

In subsequent analysis, we will need the number of SBs produced per formation of a unit stellar mass ( $\equiv \kappa$ ) that we can derive from the open cluster initial mass function. For our case, the total mass of Bhattacharya et al. (2022) catalog is  $137\,514 M_{\odot}$ , indicating that  $\kappa = 1/137\,514 \approx 7.3 \times 10^{-6} M_{\odot}^{-1}$  SBs are formed per unit stellar mass formation.

### 3. Dynamical coupling of a SB with its environment

An evacuated cavity within the interstellar gas introduces a perturbation into the local galactic potential which alters the trajectories of particles making up the ambient medium (e.g. stars, dark matter). In the case of a non-zero relative velocity between the SB and the ambient medium, this effect manifests resembles the more familiar case of dynamical friction due to a massive object (perturber), by giving rise to an energy/momentum exchange between the perturber and its surroundings.

For the dynamical friction perspective, the main difference between a massive perturber and the SB is that in the latter case, mass is merely displaced from its interior to the SB edges, hence inflating the SB and introducing zero net mass into the environment. For the idealized spherically symmetric SB and the Newton's shell theorem, the SB has no dynamical effect on particle trajectories outside its own boundaries. However, Within the SB, the same theorem implies that the perturbation to a particle's trajectory arises due to the missing mass within the spherical

region interior to the particle's radial coordinate relative to the SB center, i.e. the particle experiences an acceleration

$$\vec{a} = -\frac{GM(<r)}{r^3} \vec{r}, \quad (12)$$

where

$$M(<r) = \int_0^r 4\pi r'^2 \rho^* dr' = -\frac{4\pi r^3 \rho_{\text{env}}}{3}. \quad (13)$$

The last part of equation holds only in case of interiors of the SB.

Compared with the case of a massive object propagating through a medium, there are a few significant differences when considering dynamical friction with SB as the perturber:

1. Since the effective perturbing mass is negative, the particle trajectories tend to diverge rather than converge when traversing the SB. As a result, the wake behind the perturber is under-rather than overdense relative to the unperturbed state.
2. The spatial extent of SB's dynamical effect is limited to its own size, in contrast to a massive perturber in which case its influence formally extends to infinity. Therefore, no divergence arises when computing the energy/momentum exchange within an extended medium and no factor resembling the Coulomb logarithm appears in the final expression.
3. In contrast with most massive perturbers, the SB can evolve on timescales of interest for the dynamical friction problem, i.e. the size of the SB at the time of entry and exit of a given particle is generally different. As a result, the encounter is not conservative even in the reference frame of the SB. This effect can dominate the energy exchange compared with interaction with an unevolving perturber, where only momentum is exchanged in the perturber frame (in the limit  $m \ll M$ ).

The acceleration field for a particle at different times and locations within the evolving SB is shown in Figure 3. In keeping with the above discussion, the acceleration peaks near the inner edge of the SB wall where the interior (missing) mass is maximal. However, from the perspective of dynamical coupling between the SB and the environment, a more relevant quantity is the net energy gain or loss of a particle during the entire time spent within the SB. We show in Appendix A.2 that in the frame of the SB, this is determined by the relative radii of the SB at the time of entry and exit of the particle; if  $R_{\text{exit}} > R_{\text{enter}}$ , then net energy gain is positive and vice versa (see Eq. A.14). Since the SB evolves through both expansion and contraction phases, one can see that the dynamical friction force can have either sign even in a uniform medium, in contrast with a massive perturber.

The change of a star's velocity parallel to its initial direction as it traverses the SB is shown in Fig 5, for different impact parameters and phases in the SB evolution at the time of entry. At early entry times and for a sufficiently rapidly moving star (upper panel), we have  $R_{\text{exit}} > R_{\text{enter}}$  and the velocity gain is positive regardless of the impact parameter  $b$ . In contrast, stars that enter the SB in later phases will be able to traverse it only when the latter has already evolved well into the contraction phase; in this case, whether the ratio  $R_{\text{exit}}/R_{\text{enter}}$  is above or below unity depends on the impact parameter, with lower values of  $b$  resulting in longer residence times inside the SB, lower values of  $R_{\text{exit}}/R_{\text{enter}}$ , and a greater energy loss.

Stars with lower velocities than the characteristic expansion/contraction speed of the SB will in most cases experience

a net loss of energy and momentum<sup>1</sup>, since the SB will have had time to complete the expansion phase and contract to a size  $R_{\text{exit}} < R_{\text{enter}}$  by the time the star exits it (Figure 5, lower panel).

Whether the energy gain or loss of a given star is significant compared with its initial kinetic energy is seen from Eq. (A.14), which can be written as

$$\frac{v_{\text{out}}^2}{v_{\text{in}}^2} = 1 + \frac{[v_{\text{ch}}^2(R_{\text{exit}}) - v_{\text{ch}}^2(R_{\text{enter}})]}{v_{\text{in}}^2}, \quad (14)$$

where  $v_{\text{in}}$  and  $v_{\text{out}}$  refer to the stellar velocities at the time of entry and exit, respectively, and  $v_{\text{ch}}(r) = \sqrt{8\pi G \rho_{\text{env}} r^2 / 3}$ . Thus stars with  $v_{\text{in}} \gg \max[v_{\text{ch}}(R_{\text{enter}}), v_{\text{ch}}(R_{\text{exit}})]$  only obtain a minor correction to their initial energy and vice versa (unless, by chance,  $R_{\text{enter}} \approx R_{\text{exit}}$ ). The same applies to their trajectories, hence  $v_{\text{ch}}$  delineates the boundary between the regime where the phase space density is only slightly deformed by the SB and the collision-like regime whereby stars are displaced by a considerable distance within phase space.

### 3.1. A single SB in an environment

The total momentum transfer between a SB and a stellar population is found by integrating over the phase space of stars and SB lifetime and can be expressed as

$$\Delta \vec{P} = \int \Delta \vec{p} dF_{\text{in}} dS_{\text{b}} dt_{\text{in}}, \quad (15)$$

where  $\Delta \vec{p}$  is the momentum transfer from a single encounter,  $dF_{\text{in}}$  is the flux of stars through the unit area of the SB surface,  $dS_{\text{b}}$  is the surface element (see Eqs. (A.16) and (A.19) in Appendix A.2.1), and  $t_{\text{in}}$  is the entry time.

Note that in general the stellar flux  $F_{\text{in}}$  through the SB surface depends on the location on said surface; in fact, obtaining a nonzero value for  $\Delta \vec{P}$  relies on this being the case (otherwise the integral in Eq. (15) vanishes by symmetry). Typically this reflects the relative motion between the SB and the stellar component, whereby more stars are encountered on one hemisphere of the SB. If there exists a frame in which the stellar distribution is approximately homogeneous and isotropic, then  $\Delta \vec{P}$  is nonzero only if the SB is moving relative to this frame. From symmetry considerations one finds that the momentum transfer  $\Delta \vec{P}$  is parallel to the direction of the SB's motion in this frame. In contrast with the classical massive perturber, however,  $\Delta \vec{P}$  along this direction can take either sign depending on the specific parameters.

To illustrate the momentum exchange between the SB and the stellar population, consider an idealized configuration in which a spherical SB with a well-defined (thin) edge moves through a homogeneous stellar field with a Maxwellian velocity distribution. Such setup allows a semi-analytic treatment outlined in Appendix A.2.1, which can serve as a validation of the full numerical model.

Figure 6 shows the momentum gain experienced by stars as a function of their entry time, multiplied by the rate at which they are entering the SB at that time; the total gain/loss  $\Delta \vec{P}$  over the SB lifetime is found by integration over  $t_{\text{enter}}$ . In broad terms, the stellar population experiences a net momentum gain (along the direction of the SB propagation) in the early phases of the SB

<sup>1</sup> Here we are referring to stars with velocities directed towards the SB interior, rather than those with outward-directed velocities that are caught up by the expanding SB (which constitute a minority compared with the former in terms of how many enter the SB).

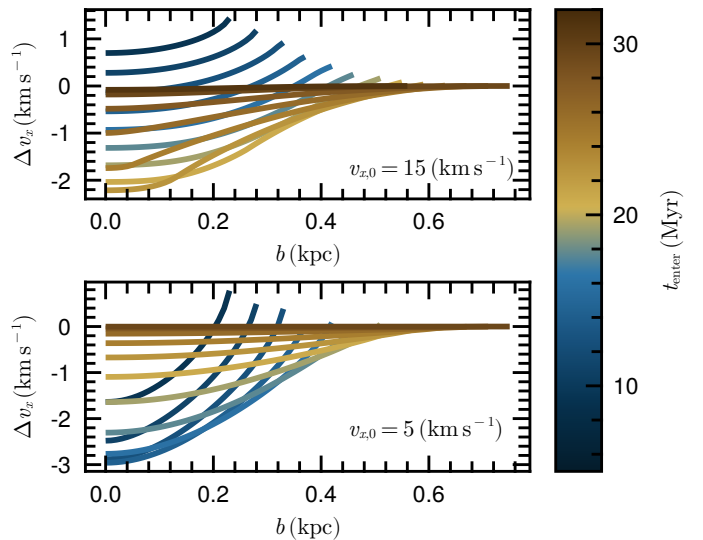


**Fig. 5.** The velocity changes for stars passing through the SB. The top part of the panel shows stars that enter the SB with  $\mathbf{v}_0 = (15, 0) \text{ km s}^{-1}$ , while in the bottom half  $\mathbf{v}_0 = (5, 0) \text{ km s}^{-1}$ . The colour depicts the time the star enters the SB.

evolution and vice versa. This is consistent with the discussion in the previous section, whereby a star entering the SB in its growing phase will more frequently have  $R_{\text{exit}}/R_{\text{enter}} > 1$  and gain energy by the encounter. Expectedly, most of the momentum exchange is done by stars that traverse the SB when the latter is not far from its maximal size, while stars entering either very early or very late in the SB life cycle have  $R_{\text{enter}}, R_{\text{exit}} \ll R_{\text{max}}$  and their energy/momentum transfer is correspondingly small (see Eqs. A.13 and A.14).

Finally, the angular momentum can be acquired analogously as momentum. The integration is done over the angular momenta changes of individual particles ( $\Delta L'_z$ ):

$$\Delta L_z = \int \Delta L'_z dF_{\text{in}} dS_{\text{b}} dt_{\text{in}}. \quad (16)$$

### 3.2. Including all the SBs

SBs do not usually occur as single isolated entities; instead, in most star-forming galaxies, they are generated at a certain rate throughout the gas disc. The resulting dynamical coupling between the stellar and gas components can be described by some average momentum exchange rate between the two components per unit disc area. Specifying to the case of circular orbits within the gas disc, the exchange can be characterized in terms of either linear or angular momentum, collectively denoted as  $\Delta \Theta = \{\Delta P_x, \Delta L_z\}$ .

#### 3.2.1. Transfer of linear momentum

First, let us consider the exchange of linear momentum, taking  $\Delta \Theta = \Delta P_x$ . Within a disc-like environment, we consider a gas slab with area  $A$  and height  $h$  and denote the rate of SB formation per unit area as  $f_{\text{b}}$ . As the star-formation activity is concentrated towards the midplane of the gas disc (region of coldest gas), we assume the SB centres are likewise in the midplane, disregarding any vertical variation.

The rate of SB formation in the above region is therefore  $f_{\text{b}}A$ , each SB contributing an exchange of momentum  $\Delta P_x$ . This

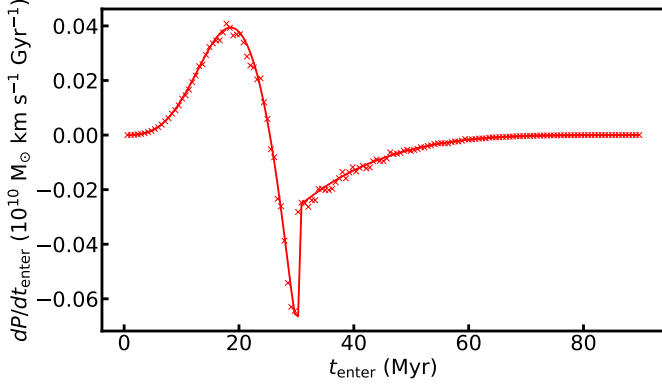


**Fig. 6.** Momentum exchange rate between the stellar population and an idealized thin-edged SB with constant expansion and contraction velocities  $v_{\text{exp}} = 20 \text{ km s}^{-1}$  and  $v_{\text{col}} = 10 \text{ km s}^{-1}$ , respectively, and expansion phase duration of 30 Myr. The ambient gas density is  $0.015 M_{\odot} \text{ pc}^{-3}$ . The stellar density is  $0.1 M_{\odot} \text{ pc}^{-3}$ , with a Maxwellian velocity distribution with  $\sigma = 25 \text{ km s}^{-1}$ . The relative velocity between the SB and the stellar distribution is  $v_b = 10 \text{ km s}^{-1}$ . The solid line shows the semi-analytical solution given by Eq. (A.21), the symbols correspond to the full numerical solution.

yields a momentum gain rate of gas within the region  $-f_b A \Delta P_x$  and a corresponding rate for the stellar population (with opposite sign), or equivalently, an effective force per unit area,  $dF_x/dA = -f_b \Delta P_x$ .

The gas mass per unit area (i.e. surface density) is  $\Sigma_{\text{gas}} = \rho_{\text{gas}} h$ . Hence the gas deceleration rate is

$$s \equiv \frac{dv_{\text{gas}}}{dt} = -\frac{1}{\rho_{\text{gas}} h} \frac{dF_x}{dA} = -\frac{f_b \Delta P_x}{\rho_{\text{gas}} h}. \quad (17)$$

### 3.2.2. Transfer of angular momentum

The angular momentum gain/loss of the gas disc can be evaluated by taking  $\Delta\Theta = \Delta L_z$ ; the effect can be characterized by the relative rate of change of specific angular momentum of a gas element, or equivalently, the rate of radial migration of a disc annulus.

The former essentially yields a timescale (more precisely, its inverse) of significant angular momentum change to take place,

$$\zeta \equiv \frac{\dot{L}_z}{L_z} = -\frac{\Delta L_z f_b}{\Sigma_{\text{gas}} R v_c}, \quad (18)$$

where  $R$  is the galactocentric distance, and we have assumed that the rotational velocity is very close to the circular speed  $v_c^2 = -R \partial \Phi / \partial R$  determined by the galactic potential.

To determine the resulting radial migration speed, one can use the continuity and angular momentum conservation equations for the gas disc in cylindrical coordinates,

$$\frac{\partial}{\partial t} \Sigma_{\text{gas}} + \frac{1}{R} \frac{\partial}{\partial R} (R \Sigma_{\text{gas}} v_R) = 0. \quad (19)$$

and

$$\frac{\partial}{\partial t} (\Sigma_{\text{gas}} R^2 \Omega) + \frac{1}{R} \frac{\partial}{\partial R} (R \Sigma_{\text{gas}} v_R R^2 \Omega) = T_A, \quad (20)$$

respectively, where  $v_R$  is the radial velocity and the right-hand side is the imposed torque per unit surface area.  $\Omega$  denotes the

angular velocity. Using Eq. (19), the angular momentum equation can be rewritten in the form

$$v_R \frac{\partial}{\partial R} (R^2 \Omega) = \frac{T_S}{\Sigma_{\text{gas}}} \equiv T, \quad (21)$$

where  $T$  is the torque per unit mass and we have assumed  $\partial(R^2 \Omega) / \partial t = 0$ , which is justified if the orbital velocity only depends on  $R$ .

In the present context, the torque per unit mass from dynamical friction is  $T = \Delta L_z f_b / \Sigma_{\text{gas}}$ , whereby Eq. (21) yields

$$v_R = \frac{\Delta L_z f_b}{\Sigma_{\text{gas}} \partial(R^2 \Omega) / \partial R} = \zeta R \left[ 1 + \frac{d \ln v_c}{d \ln R} \right]^{-1}, \quad (22)$$

where we have used  $v_c = R \Omega$ .

### 3.2.3. The SB formation rate

Both SB influence estimators (17) and (18) depend on the SB rate, to which we provide three estimates: from direct observations, from the Kennicutt-Schmidt relation and from the SB saturation limit.

Ehlerová & Palouš (2013) measured the surface density of SBs with radius over 100 pc in Solar Neighbourhood to be about 4 per  $\text{kpc}^2$ . To convert this into SB rate, we use the lifetime of SB  $t_{\text{end}} = 71.6 \text{ Myr}$  (see Sect. 2.2), from which during 31.6 Myr it has an inner radius exceeding 100 pc. To have 4 SBs per  $\text{kpc}^2$ , the formation rate of SBs should be  $f_b = 127 \text{ kpc}^{-2} \text{ Gyr}^{-1}$ .

Kennicutt-Schmidt relation can be used for SB rate estimates as well. In Sect. 2.3, we defined the conversion rate ( $\kappa$ ), showing how many SBs form per formed stellar mass. Hence, we can convert the surface density of the star formation rate to the SBs formation rate by simple multiplication. Using the Kennicutt-Schmidt relation for non-starburst galaxies from de los Reyes & Kennicutt (2019) with the surface density of gas  $13.6 M_{\odot} \text{ pc}^{-2}$  (McKee et al. 2015) we obtain the rate of SBs  $f_b = 42 \text{ kpc}^{-2} \text{ Gyr}^{-1}$ .

If the formation rate of SBs is high and the lifetime of SBs long, they start to overlap, and new ones are forming in the edges of older SBs (Barnes et al. 2022). This does not allow the SB to complete its full evolution cycle, and our approximation of a single SB influence breaks down. Let us estimate the SB rate when the saturation of independent SBs occurs. We assume that a higher SB rate does not produce a larger  $\Theta$  transfer. We derive the saturation limit by simulating the formation of SBs at random positions and times, and  $f_b$  measures the number of random points inside of SBs (defined as the distance from a random point to the SB centre is less than  $R_m$ ) on average. At SB formation rate of  $f_b = 25 \text{ kpc}^{-2} \text{ Gyr}^{-1}$  the number of overlapping SBs will be over unity on average, and we use this rate as the saturation limit. Figure 7 shows the saturation level of our simulation.

Considering all these estimates are diverse and almost independent, we choose the most conservative one for further analysis:  $f_b = 25 \text{ kpc}^{-2} \text{ Gyr}^{-1}$ . Changing the  $f_b$  changes the secular evolution speed proportionally.

## 4. Examples of SBs in various environments

### 4.1. SB in a homogeneous isotropic environment

This section shows the amount of de-acceleration ( $s$ ) SBs induce in gas. We assume a homogeneous and isotropic environment, being an approximation to a more realistic environment. First, we solve the SB influences numerically using (17), and then construct an approximation formula to simplify its future evaluations.

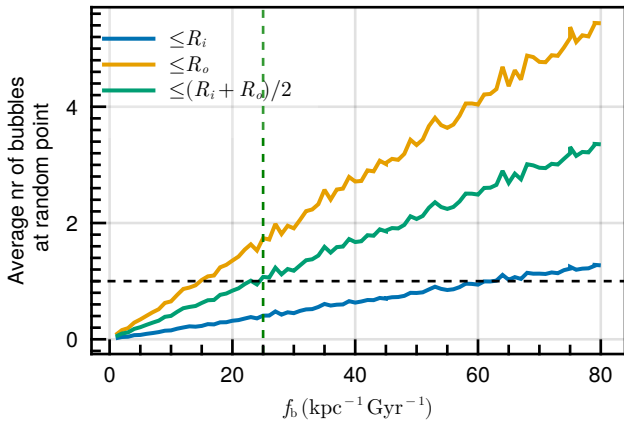


**Fig. 7.** The average number of SBs that are in a random point based on simple numerical simulation.

**Table 1.** The parameters for determining the level of the influence to the gas slab by the stars via SBs.

	Default value	Comment
$v$	$10 \text{ km s}^{-1}$	The velocity of SB with respect to gas This and the next parameter are used in phase space density in Eq. (A.17)
$\sigma$	$20 \text{ km s}^{-1}$	The velocity dispersion of the stars
$v_{\text{col}}$	$10 \text{ km s}^{-1}$	Sets the SB collapse in Eqs. (2) and (3)
$s_r$	1.19	SB scaling defined in Eq. (4). With $v_{\text{col}}$ , it fixes SB lifetime $t_b = 71.58 \text{ Myr}$
$\rho_{\star}$	$0.1 M_{\odot} \text{ pc}^{-3}$	Stellar density used in (A.17)
$\rho_{\text{gas}}$	$0.015 M_{\odot} \text{ pc}^{-3}$	Density of the gas hosting SB
$f_b$	$25 \text{ kpc}^{-2} \text{ Gyr}^{-1}$	The rate SBs form, see Sect. 3.2.3

The setup of the environment is a slab of gas, which we complement with homogeneous stellar distribution with isotropic velocities.  $v$  denotes the average velocity between the gas and stars, an analogue to asymmetric drift;  $\sigma$  denotes the stellar velocity dispersion. The calculations prescription was in Sect. 3.2.1, and the implementation parameters are in Table 1.

Figure 8 shows the resulting de-acceleration of the gas slab, both in kinematic and SB property aspects. For the context, we look at a MW-like galaxy that formed its discs around redshift 1.5 – 2 (van der Wel et al. 2014), indicating the discs have time to modify their discs about 10 Gyr. If we assume a flat rotation curve with a velocity plateau of  $230 \text{ km s}^{-1}$ , then during that time, the gas can migrate from due to SB  $\approx 10s/230$ , or 20% if  $s = 5 \text{ km}^2 \text{ s}^{-2} \text{ kpc}^{-1}$ . The evaluation assumes a homogeneous host environment, which we discard in the next section. Figure 8 shows that the highest impact comes from the parameter space where the stellar disc is cold, its velocity dispersion is below  $10 \text{ km s}^{-1}$ , but with some dependence on the relative velocity of the gas disc and the stellar one. The bottom panel show the dependence on the SB properties, with slow-collapsing SB being more efficient in transferring momentum – longer age extends the time of momentum transfer. Analogously, the larger size (described by  $s_r$ ) increases the cross-section of the SB, allowing more stars to transfer their momenta. Also, larger SBs have larger displaced gas mass and they provide higher accelerations (see Sect. 2).

To evaluate the de-acceleration with more ease, we fitted an empirical approximation formula to the top plane in Fig. 8. We made an analytic approximation for the simple case using *SymbolicRegression* package (Cranmer 2023) in Julia (Bezanson et al. 2017). The mean and standard deviation of the residuals of

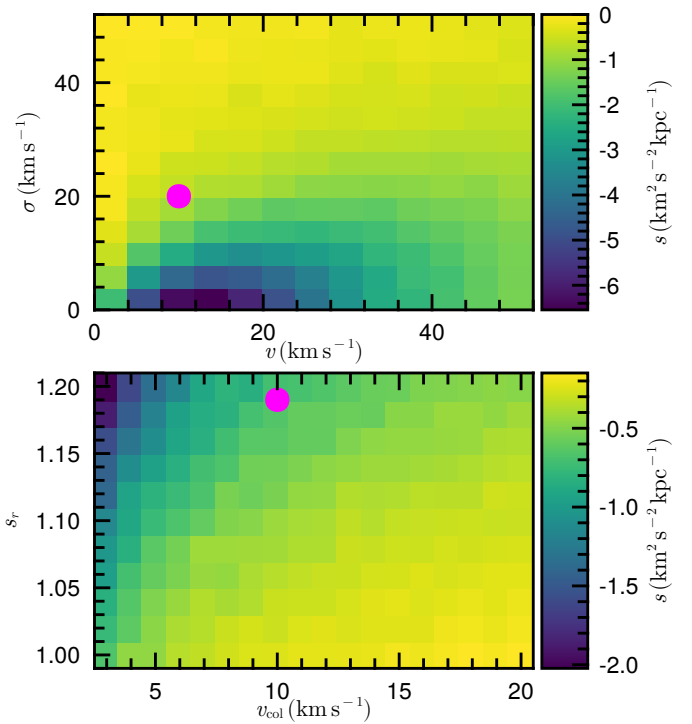


**Fig. 8.** The de-acceleration  $s$  in a homogeneous environment. The long-term effects can be estimated using relation  $\text{km s}^{-1}$  per Gyr as it approximates  $\text{km}^2 \text{ s}^{-2} \text{ kpc}^{-1}$ . The top panel shows the dependence of  $s$  on the kinematical parameters of the homogeneous environment: the velocity and velocity dispersion. The magenta point shows the difference between MW gas and stellar disc values. The bottom panel shows the dependence on the SB parameters of collapse speed and scaling, with kinematic parameters  $v$  and  $\sigma$  fixed at the magenta point in the top panel. The de-acceleration field can be approximated using Eq. (23).

the fit is  $-0.0013 \text{ km}^2 \text{ s}^{-2} \text{ kpc}^{-1}$ ,  $0.257 \text{ km}^2 \text{ s}^{-2} \text{ kpc}^{-1}$ . The best model has the form

$$s_{\text{approx}} = \frac{v_{\text{bub}} + \sigma + a_1}{a_3(v_{\text{bub}} - a_2) \left[ a_5 + \exp\left(\frac{\sigma + a_4}{v_{\text{bub}}}\right) \right]}, \quad (23)$$

where  $a_1 = -112 \text{ km s}^{-1}$ ,  $a_2 = -1.64 \text{ km s}^{-1}$ ,  $a_3 = 0.650 \text{ km}^2 \text{ s}^{-2} \text{ kpc}^{-1}$ ,  $a_4 = 5.94 \text{ km s}^{-1}$ , and  $a_5 = -0.217$ . This equation assumes that the velocities are in  $\text{km s}^{-1}$ , distances in kpc and the resulting de-acceleration in  $\text{km}^2 \text{ s}^{-2} \text{ kpc}^{-1}$ .

## 4.2. SBs in a test-galaxy

A homogeneous environment can approximate regions without a steep density gradient and host acceleration field. But the orbits in a galaxy can have a circular nature, and they can produce mismatches with the approximation. In this section, we characterise a situation where  $\Theta = L_z$ , describing the SB effects by changes in angular momentum.

### 4.2.1. Underlying galaxy

The numerical estimations of the order of magnitude effects require specifying a galaxy. We use simple analytical potential for dynamical model evaluation and resemble a disc galaxy.

The galaxy has two density components: DM is described with Navarro Frenk White (NFW) profile (Navarro et al. 1996), and stellar distribution is described with Miyamoto-Nagai (MN)

profile (Miyamoto & Nagai 1975). The gas disc is assumed to produce an insignificant contribution to total density, and hence, its contribution to gravitational potential is neglected. The MN profile has the potential

$$\Phi_{\text{MN}} = \frac{-GM_{\text{MN}}}{\sqrt{R^2 + \left[ a_{\text{MN}} + \sqrt{z^2 + b_{\text{MN}}^2} \right]^2}} \quad (24)$$

The chosen values to MN profile were  $a_{\text{MN}} = 3.0$  kpc,  $b_{\text{MN}} = 0.4$  kpc,  $M_{\text{MN}} = 7.11 \times 10^{10} M_{\odot}$ . The NFW profile has density in the form of

$$\rho = \frac{\rho_{\text{NFW}}}{\frac{r}{R_{\text{NFW}}} \left( 1 + \frac{r}{R_{\text{NFW}}} \right)^2} \quad (25)$$

with the parameter values  $\rho_{\text{NFW}} = 0.001 \times 10^{10} M_{\odot} \text{ kpc}^{-3}$  and  $R_{\text{NFW}} = 15$  kpc.

To evaluate the SB influence on the galaxy, we need to know the stellar and DM particle kinematics. They are found from Jeans equations (Jeans 1915) by assuming stationarity and cylindrical or spherical symmetry for the disc and DM halo, respectively.

The first equation for solving disc kinematics is the radial Jeans equation

$$\frac{\partial(\rho\sigma_R^2)}{\partial R} = -(1 - \beta^2)\rho \frac{\partial\Phi}{\partial R} - \frac{1 - \alpha^2}{R}(\rho\sigma_R^2), \quad (26)$$

with simplifying assumptions that tangential dispersion is proportional to radial one and rotational velocity to circular one:

$$\sigma_{\theta} = \alpha\sigma_R \quad (27)$$

$$v_{\text{rot}} = \beta v_{\text{circ}}. \quad (28)$$

In our applications, the velocity ellipsoid is slightly elongated in the radial direction,  $\alpha = 0.8$ , and the asymmetric drift (the relative speed between circular velocity and rotational one) is about  $\approx 10 \text{ km s}^{-1}$  as we chose  $\beta = 0.95$ . The vertical motions originate from solving the vertical Jeans equations by assuming that the tilt term in Jeans equations is zero:

$$\frac{\partial(\rho\sigma_z^2)}{\partial z} = -\rho \frac{\partial\Phi}{\partial z}. \quad (29)$$

We solved the equations using the Runge-Kutta-Fehlberg method by integrating  $\rho\sigma_r^2$  or  $\rho\sigma_z^2$  along the coordinate axis<sup>2</sup> and then solving for the kinematical property.

By assuming non-rotating isotropic velocity distribution, the solution for the spherical Jeans equations for the DM kinematics was provided in Kipper et al. (2019). Our aim is also to test if the rotation of DM influences the angular momentum transfer by gas. We wanted to achieve a situation where as many other parameters as possible aside from the rotation are shared with the non-rotating solution. The rotation can be induced by modifying the spherical solution by lowering one side of the  $v_{\text{rot}}$  distribution ( $p_{\text{rot,DM}}$ ) on one side and increasing it by the same amount on the other side similar to Joshi & Widrow (2023). Effectively, it means that the overall potential and density remain the same if the rotational direction of a fraction of stars is switched<sup>3</sup>. Factor  $p_{\text{rot,DM}}$  describes the modification of the distribution function

$$f_{\text{rot}} = \frac{1}{1 + \exp(-kx)} - \frac{1}{2}, \quad (30)$$

<sup>2</sup> The characteristic aligns with coordinates.

<sup>3</sup> Technically, this produces a valid solution for the solved point but loses the validity of isotropy in other radii. For the current application, it is a suitable approximation.

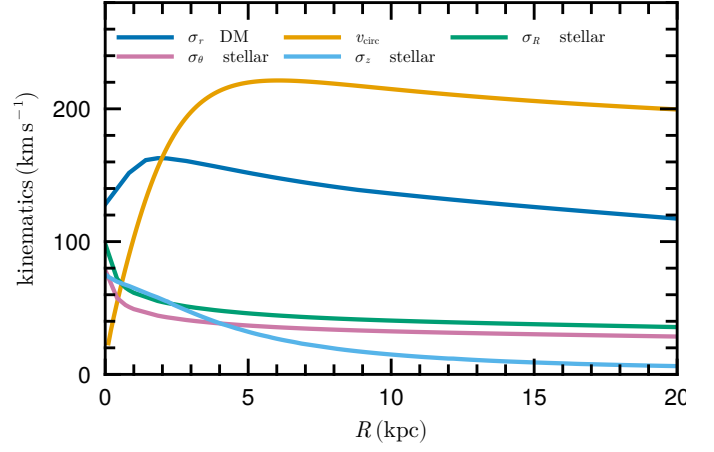


**Fig. 9.** The kinematic solution of the test-galaxy from solving the Jeans equations. The rotation curve of the disc is  $\beta = 0.95$  times the circular velocity curve.

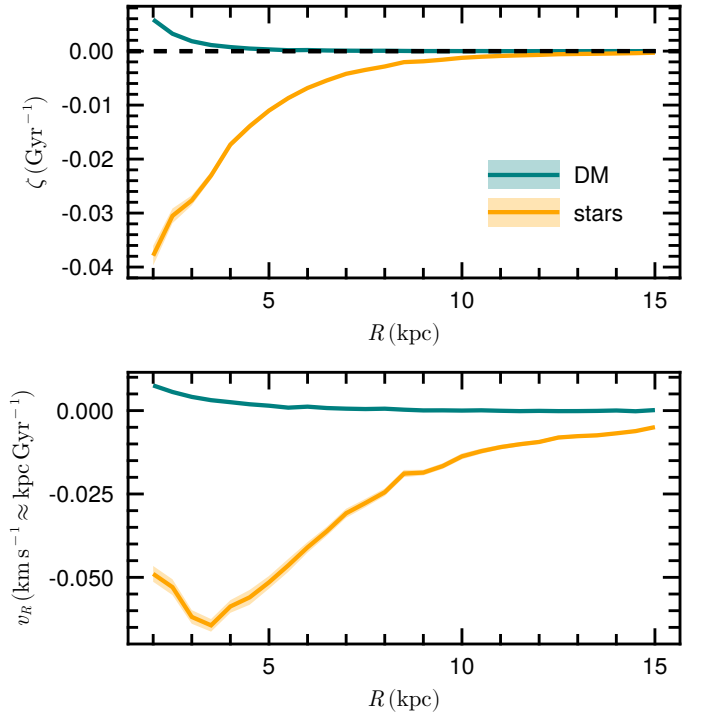


**Fig. 10.** The dependence of gas disc expansion due to SBs both in terms of relative angular momentum change (top panel) that is defined with Eq. 18 and expansion speed (bottom panel).

with  $x \equiv |v_{\text{rot}}|/\sigma_{\text{DM}}$ . The  $p_{\text{rot,DM}}$  is multiplied by  $1 \pm f_{\text{rot}}$ , depending on if  $v_{\text{rot}}$  is positive or not. In the implementation, the  $k$  equals  $\pm 5$ , which transforms the mean value to  $\pm 0.37\sigma$ . The solution of kinematics is in Fig. 9.

#### 4.2.2. The gas disc changes

Figure 10 shows the influence of the SBs on the gas disc in two representations: relative loss of angular momentum and radial velocity. We note two important things here. Firstly, the strong radial dependence in the inner region of the galaxy. The innermost region was not calculated as the SB would not fit the region without breaking down the shape assumptions. Secondly, the opposite sign of the contributions by the DM and stellar component.

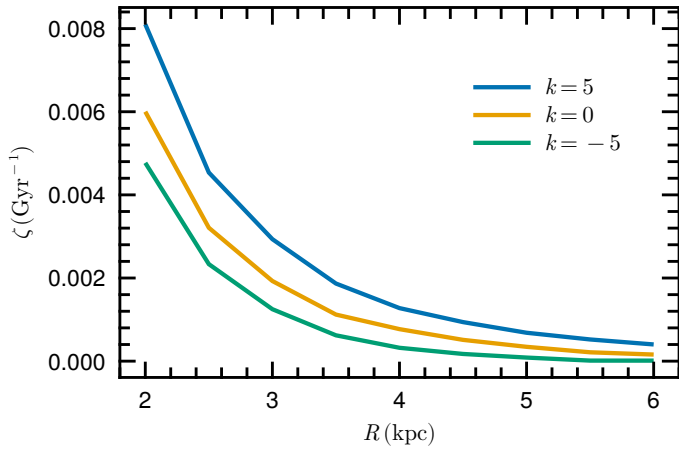


**Fig. 11.** DM rotation influence to the transfer of angular momentum between DM and the gas disc ( $\zeta$ ). Different  $k$  values correspond to different rotations, with value  $\langle v \rangle = 0.37\sigma$ , the dispersion of DM halo is shown in Fig. 9.

This is specific only to the region where particles pass through the SB very fast and the gravitational potential is cylindrical and does not occur in the homogeneous and isotropic medium. There are multiple effects in play simultaneously, so pinpointing the exact culprit for this effect is unfeasible in the current study.

The rotation of the DM profile might produce some changes in the stellar disc, e.g. Herpich et al. (2015); Kataria & Shen (2022); Li et al. (2023). One physical reason is that the dynamical friction is sensitive to the kinematics of the particles, not only density (Chandrasekhar 1943). Therefore we investigated the role of DM rotation on the gas disc via the dynamical friction. Figure 11 shows the difference between different DM rotation models. We conclude that the contribution from DM kinematics exists but is weak.

## 5. Discussion

### 5.1. Observational verification of the SB profile

In Sec. 2.1, we described the density profile of a SB as derived in Y17. Here we aim to verify the density's consistency with the observations. Watkins et al. (2023) analysed the galaxy NGC 628 in terms of its SB content from the observations from the PHANGS46–JWST using the MIRI's F770W filter. We take advantage of this observation and focus on the SB situated at approximately (3 kpc), south-east from the center of this galaxy. This SB is an ideal example of such processes as it has an almost circular shape.

We measure the surface brightness in circular regions from the centre of the SB, matching our coordinate centre. Y17 results assume initially homogeneous gas distribution, but in our case, this is not fully satisfied if we want to investigate the ISM regions further than the extent of the SB. To test if this is an issue, we measure the surface brightness only in a well defined shell-like structure as seen in the JWST image, also done in the work of Mayya et al. (2023). This approach accounts for the influence of various external factors, including the collapse of edges, gas diffusion, and other effects.

We generate the intensity of the profile from the intensity map of the image by averaging intensities at different radii from the shell centre. Thereafter, we bin these radii so that we can get a smoother profile. For the binned data, we calculate the mean and the error of the mean by bootstrapping Efron (1979). This

gives us the observed surface brightness profile within errors, which is proportional to the density ( $\rho$ ) profile given by Y17. The theoretical density profile is approximated in 2.1 following the Y17 simulation. This simulation assumes a homogeneous environment for all the initial conditions. The observations are more complex as the interstellar medium and gas outside the SB are not homogeneous as well and there are other effects contributing, such as the higher gas density on the spiral that one side of the SB resides or some higher rates of star formation at the edges of the SB from the pressured gas or other specific gas properties. We denote this conversion factor between the surface density of the Y17 fiducial profile and the surface brightness of the observations by  $C$ . To exclude ISM effects in the observations, we take into account radii up to 0.7 kpc, a bit further than the well-defined luminosity shell of the profile. Additionally, the observations have a background intensity that we denote as  $B$ .

The conversion between the line of sight and SB-centric coordinate in a galaxy is  $l = \pm\sqrt{r^2 - R^2}$ , where  $r$  is the 3D distance from the center of the SB and  $R$  is the distance from the center of the circle as measured in the photometric image.

Thus, the line-of-sight integral is defined as:

$$I(R) = C \int_{-l_{\text{lim}}}^{+l_{\text{lim}}} \rho[r(l)] dl + B \quad (31)$$

This gives us five free parameters, three that are results of the observational image,  $C$ ,  $B$ ,  $l$ , and two that describe the SB, its expansion time  $t$  and the scaling factor  $s_r$  (analytically described in Sec. 2.2). These parameters are modelled within large and uniform priors. We aim to match the observed data with the theoretical model by following a Bayesian approach (Laplace 1774). We consider errors as coming from the standard deviation derived from bootstrapping plus a systematic uncertainty to account for the fact that the SB is not isolated or in a homogeneous environment.

The following equation gives us the likelihood of the posterior. We used  $10^5$  iterations in an adaptive Monte Carlo scheme provided by Julia, as implemented by Vihola (2020).  $I_{\text{obs}}$  denotes the surface brightness as coming from the JWST image in the radii bins, and the MCMC inference estimates the free parameters for the  $I_{\text{model}}$ , and  $\Delta I_i$  represent the associated errors.

$$\log \mathcal{L} \propto -0.5 \sum_{i=1}^N \left[ \left( \frac{I_{\text{obs},i} - I_{\text{model},i}}{\Delta I_i} \right)^2 \right] \quad (32)$$

The constraints of the time of the expansion of the SB to  $t_{\text{obs}} = 0.030 \pm 0.002$  Gyr indicate that the time of the observation of the specific SB's evolutionary stage is at its biggest peak before starting to shrink. We also constrained the scaling factor to  $s_r = 1.18 \pm 0.04$ , translating to  $\approx 230$  progenitor supernova explosions. For the rest of the parameters, we obtained the line-of-sight distance  $l_{\text{lim}} = 0.37 \pm 0.02$  kpc and the luminosity background information of the JWST image as  $B = 10.79 \pm 0.03$  Jy/sr. The latter is within the measurements consistent with regions outside the galaxy.

As demonstrated in Fig. 12, the theoretical model closely matches the observational data, providing an agreement between the approach of the Y17 profile and the observed data. This verifies that the theoretical density profile from Y17 describes accurately the SB phenomena.

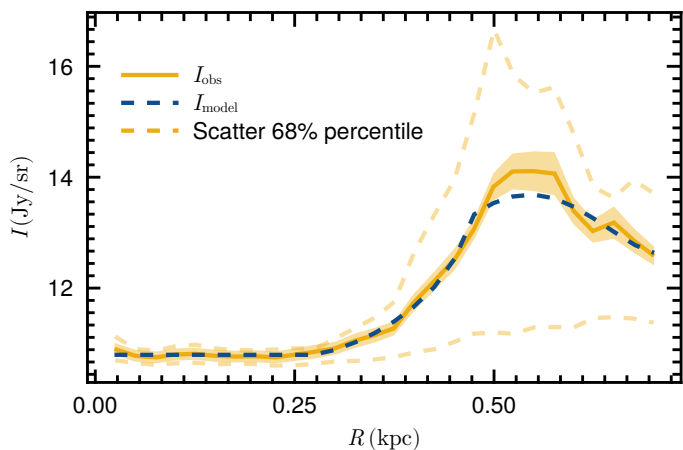


**Fig. 12.** Comparison between the surface brightness from JWST image and the surface brightness as it comes from Y17 best fit of the model. The observational flux of the SB (gold line) is plotted between three sigma (light gold dashed lines) and the standard deviation plus the systematic error of the bootstrap analysis for the binned data. The best fit of the model incorporating the five free parameters is superimposed on them (blue dashed line)

## 5.2. Robustness of the assumptions and approximations

Our analysis relies on a few assumptions about the SB itself, its environment and the stars interacting with it. The SB description is based on the Y17 simulation and their assumptions about the SB propagate here. Their dominant assumptions are homogeneous initial gas distribution with gas density analogous to the solar neighbourhood and the stars exploding near the centre being distributed uniformly in time.

### 5.2.1. Environment assumptions

The gas distribution in real galaxies is not homogeneous: radial and vertical gradients of the gas density contradict our assumptions. The Sersic profile describes the HI surface brightness distribution, whereas the Sersic index characterises the steepness or gradient of the profile. Low values indicate nearly constant core with truncation, and large values ( $\sim 4$ ) indicate cuspy profiles. The Sersic index of averaged matter distribution of spirals from the THINGS survey is between 0.18 – 0.36 (Brinks & Portas 2017), showing the gradient of the gas disc to be much shallower than typical stellar disc (Sersic index  $\sim 1$ ) and thus the homogeneity assumption in the radial direction is a good approximation. The vertical gradient of gas discs is much steeper. The scale heights of different types of gas vary between 75 pc for molecular gas to 3000 pc for hot ionised medium (Ryden & Pogge 2021). The highest contribution comes from the warm neutral medium with the scale height of  $\sim 300$  pc, which corresponds to the fiducial SB inner radius at the maximum extent. To see if the disc-height limited profile still matches the theoretical one, we modelled observations with our used SB model. In Sect. 5.1, we show that the profiles match best when the integration extent over the line of sight is 370 pc, which slightly exceeds the scale height of the gas disc, indicating that the SB almost fits the gas discs.

We intrinsically assume that the shape of the SB remains spherical. One reason for deviations from sphericity is shearing motions from galactic rotation. We test the extent of shear distortions by assuming a flat rotation curve with  $v_0$ , the SB is at galactocentric radius  $R_0$ , the radius of SB is  $R_{SB}$  and the time

of shearing is  $\Delta t$ . In that case, the far edge of the SB can shift by  $v_0 R_{SB} \Delta t / R_0 \approx 225$  pc from the centre when assuming values  $\Delta t = 30$  Myr,  $R_0 = 8$  kpc,  $R_{SB} = 300$  pc and  $v_0 = 200$  km s $^{-1}$ .<sup>4</sup> Indeed, When trying to see if the elongation and tilt are present in observations (e.g. Barnes et al. (2023) images), we can see it for some SBs, which is a plausible deviation from our assumption. However, Binney & Tremaine (2008) showed that the gravitational potential ellipticity is in the order of  $1/3 \dots 1/2$  of the density ellipticity. Our current example has ellipticity of 0.43, which translates to potential ellipticity of 0.14  $\dots$  0.23 or axis ratio  $\approx 0.82$ . Considering other uncertainties of the SB rate, evolution and structure precision, we do not consider this deviation to be of first order importance.

The secular evolution of the gas disc due to SBs is proportional to the rate of SB formation in the galaxy; see Eq. (17) and (18). Although our estimates of the SB formation rate have a high scatter (see Sect. 3.2.3), we would like to point out the possibility that there are spatial variations of the rate within a galaxy and between the galaxies. Finn et al. (2024) show that most massive molecular clouds, producing more likely open clusters able to develop into SBs, occur more likely in prominent spirals, contrary to inter-arm regions or regions in flocculent galaxies. In the latter cases, we suspect our de-accelerations are overestimated. However, although smaller SBs have also smaller effects on the galaxy evolution (see Fig. 8), their amount is larger and their cumulative effect can be comparable.

### 5.2.2. SB assumptions

In the case of the SB physics, we assume the shape of the SB is the same as Y17 described, and it has the same scaling relation they provided. We tested the suitability of the profile in Sect. 5.1.

Although the observed and theoretical profiles match, the link between the SB and the SNe/SFR needed to create them needs a discussion. In Sect. 2.3, we adopted the approach that 100 SNe produce a stable SB and evaluated the results accordingly. Fewer SNe are also likely to make a SB, but it is not so stable. The smaller amount of SNe can be significant, e.g. Barnes et al. (2022) showed many SBs in a galaxy when looked at high resolution. We suspect the smaller ones can also transfer angular momentum but less effectively (see Fig. 8). This paper does not provide the analysis for that.

Figure 8 shows that in addition to the size of the SB, the collapsing speed ( $v_{col}$ ) strongly influences how much the SB affects the transfer of momentum. If the corresponding time of the SB is twice as fast, then the transfer efficiency reduces, but the SB rate ( $f_b$ ) increases<sup>5</sup>. Kinugawa et al. (2023) demonstrated that due to mass transfer between binaries, the time when the SNe can occur in an open cluster gets extended, possibly delaying the collapse of SBs.

## 5.3. Implications

Della Croce et al. (2023) reported that the outskirts of open clusters are expanding: outer parts faster than inner. The trend lasts for 30 Myr. Based on our description of the SB, the first 30 Myr is the expanding phase of the SB, causing an additional acceleration field; see Fig. 3. We tested the significance of the SB acceleration on a fictive open cluster by generating an open cluster

<sup>4</sup> Calculations assume there are no compensating forces, like pressure gradients, to restore the round shape.

<sup>5</sup> Here we are assuming that the limiting factor of SBs is the spatial saturation, see Sect. 3.2.3.

with mass  $10^4 M_{\odot}$ , radius 5 pc and evaluated what is the relative acceleration originating from the SB:  $|a_{\text{SB}}|/(|a_{\text{SB}}| + |a_{\text{OC}}|) = 0.18 \pm 0.09$ . The  $\pm$  describes different stars in the cluster. We conclude that SB can provide an additional acceleration field to alter the kinematics of open clusters. Still, the further acceleration does not necessarily translate to expansion but extended times in outer parts of the orbits or possibly easier evaporation.

There have been indications that the rotation of DM halo is affecting the baryonic parts of the galaxy (Herpich et al. 2015; Kataria & Shen 2022; Li et al. 2023), or the opposite (Nuñez-Castiñeyra et al. 2023). In Fig. 11, we evaluated the extent to which SBs can cause the angular momentum transfer, being up to 5% per 10 Gyr. Upon measuring the shrinking of gas discs in a galaxy absent of spirals and bars (e.g. using chemical imprints) extremely precisely, it is, in theory, possible to infer the rotation of the DM halo.

## 6. Summary

Galaxies evolve via stochastic and secular processes: two-body relaxation, virialisation, momentum transfer by spirals and bars, major mergers, minor mergers, etc. The last item in the list can provide torques via dynamical friction, changing the angular momentum of the merger with the disc. We study additional effects related to dynamical friction that are caused not by external satellites but by gas inhomogeneities – namely superbubbles (SB) introduced by multiple supernovae (SN) explosions originating from open clusters.

We characterise the SB influence by acceleration field correction originating from density field correction. We apply this correction to stellar and dark matter (DM) particle trajectories that pass through the SB and evaluate the velocity or angular momentum changes. By stacking together all the particles, including the time-dependence of the SB and counting the constant formation-destruction cycle of the SBs, we measure the extent of the dynamical friction from the SBs.

The summary of the SB influences on the galaxy are following:

- The acceleration field of the SB correction is directed outward: if the gas mass is missing from the SB centre, the correction to mass is negative, and the radial acceleration is also negative. See Sect. 2 for the derivation of the effect.
- Stars entering the SB slowly can reverse their movement direction, indicating that stars almost co-moving with the SB; see Sect. 3.
- The SB effects can be approximated empirically, see Eq. (23). We provide an analytical approximation for a gas slab in stellar distribution that is homogeneous and isotropic.
- For the test galaxy, we estimated the change to the gas disc when both the SB and the galactic potential influence the orbits of stars. The relative rate of angular momentum changes is up to  $4\% \text{ Gyr}^{-1}$ , which can account for significant changes over the galaxy's lifetime.
- The dynamical friction is a process that depends on the velocity of the host environment (Chandrasekhar 1943). As we are studying processes similar to dynamical friction, we estimated the possible contribution of the rotation of DM halo to the transfer and if this can be used to infer the kinematics of DM. The differences are in the order of  $\sim 0.3\% \text{ Gyr}^{-1}$ , or  $\sim 3\%$  over the times average disc has existed. Measuring these rates is extremely difficult, but in theory, the DM rotation influences the gas disc via SBs.
- We also discussed the assumptions related to the SB evolution and environment in the Discussion.

## Acknowledgements

We thank Punyakoti Ganeshaiha Veena for helpful discussion. The present study was supported by the ETAG projects PSG700, PRG1006 and PRG2159 This work was partially supported by the ETAG CoE grant "Foundations of the Universe" TK202 and EU twinning project EXCOSM. AT was also supported by the COST Action CA21126 - Carbon molecular nanostructures in space (NanoSpace)-COST (European Cooperation in Science and Technology).

## Data Availability

The codes and scripts used to produce these results are available in GitLab <https://gitlab.ut.ee/rain.kipper/onlybubbles>.

## References

- Barnes, A. T., Chandar, R., Kreckel, K., et al. 2022, Linking stellar populations to HII regions across nearby galaxies: I. Constraining pre-supernova feedback from young clusters in NGC1672
- Barnes, A. T., Watkins, E. J., Meidt, S. E., et al. 2023, *ApJ*, 944, L22
- Bezanson, J., Edelman, A., Karpinski, S., & Shah, V. B. 2017, *SIAM Review*, 59, 65
- Bhattacharya, S., Rao, K. K., Agarwal, M., Balan, S., & Vaidya, K. 2022, *MNRAS*, 517, 3525
- Binney, J. 2013, in *Secular Evolution of Galaxies*, ed. J. Falcón-Barroso & J. H. Knapen, 259
- Binney, J. & Tremaine, S. 2008, *Galactic Dynamics: Second Edition*
- Brinks, E., Bagetakos, I., Walter, F., & de Blok, E. 2007, in *Triggered Star Formation in a Turbulent ISM*, ed. B. G. Elmegreen & J. Palous, Vol. 237, 76–83
- Brinks, E. & Portas, A. 2017, in *Formation and Evolution of Galaxy Outskirts*, ed. A. Gil de Paz, J. H. Knapen, & J. C. Lee, Vol. 321, 235–237
- Byrne, R. A. & Fraser, M. 2022, *MNRAS*, 514, 1188
- Chandrasekhar, S. 1943, *ApJ*, 97, 255
- Cowie, L. L. & McKee, C. F. 1977, *ApJ*, 211, 135
- Cranmer, M. 2023, arXiv e-prints, arXiv:2305.01582
- de los Reyes, M. A. C. & Kennicutt, Robert C., J. 2019, *ApJ*, 872, 16
- Della Croce, A., Dalessandro, E., Livernois, A. R., & Vesperini, E. 2023, arXiv e-prints, arXiv:2312.02263
- Efron, B. 1979, *The Annals of Statistics*, 7, 1
- Ehlerová, S. & Palouš, J. 2013, *A&A*, 550, A23
- Finn, M. K., Johnson, K. E., Indebetouw, R., et al. 2024, ALMA-LEGUS II: The Influence of Sub-Galactic Environment on Molecular Cloud Properties
- García-Conde, B., Antoja, T., Roca-Fàbrega, S., et al. 2023, arXiv e-prints, arXiv:2311.07137
- Herpich, J., Stinson, G. S., Dutton, A. A., et al. 2015, *MNRAS*, 448, L99
- Huško, F., Lacey, C. G., & Baugh, C. M. 2023, *MNRAS*, 518, 5323
- Jeans, J. H. 1915, *MNRAS*, 76, 70
- Joshi, R. & Widrow, L. M. 2023, *The Formation of Bars and Warps in Rotating Halos*
- Kataria, S. K. & Shen, J. 2022, *The Astrophysical Journal*, 940, 175
- Keller, B. W. 2017, in *Superbubble Feedback in Galaxy Evolution*
- Keller, B. W., Wadsley, J., Benincasa, S. M., & Couchman, H. M. P. 2014, *MNRAS*, 442, 3013
- Kinugawa, T., Horiuchi, S., Takiwaki, T., & Kotake, K. 2023, arXiv e-prints, arXiv:2311.14341
- Kipper, R., Benito, M., Tenjes, P., Tempel, E., & de Propriis, R. 2020, *MNRAS*, 498, 1080
- Kipper, R., Tamm, A., Tempel, E., de Propriis, R., & Ganeshaiha Veena, P. 2021, *A&A*, 647, A32
- Kipper, R., Tenjes, P., Benito, M., et al. 2023, *A&A*, 680, A91
- Kipper, R., Tenjes, P., Hütsi, G., Tuvikene, T., & Tempel, E. 2019, *MNRAS*, 486, 5924
- Kormendy, J. 2013, in *Secular Evolution of Galaxies*, ed. J. Falcón-Barroso & J. H. Knapen, 1
- Kroupa, P. 2001, *MNRAS*, 322, 231
- Kuzmin, G. G. 1961, in *Publications of the Tartu Astrofizika Observatory*, Vol 33, 351–370, see an English translation as Chapter 19 in
- Kuzmin, G. G. 1963, in *Publications of the Tartu Astrofizika Observatory*, Vol 34, 9–37, see an English translation as Chapter 22 in
- Laplace, P.-S. 1774, *Memoir on the probability of causes of events*.
- Lara-López, M. A., Pilyugin, L. S., Zaragoza-Cardiel, J., et al. 2023, *A&A*, 669, A25

- Li, X., Shlosman, I., Heller, C., & Pfenniger, D. 2023, Monthly Notices of the Royal Astronomical Society, 526, 1972–1986
- Lian, J., Zasowski, G., Hasselquist, S., et al. 2022, MNRAS, 511, 5639
- Mac Low, M.-M. & McCray, R. 1988, ApJ, 324, 776
- Maxwell, A. J., Wadsley, J., & Couchman, H. M. P. 2015, ApJ, 806, 229
- Mayya, Y. D., Alzate, J. A., Lomelí-Núñez, L., et al. 2023, Monthly Notices of the Royal Astronomical Society, 521, 5492–5507
- McKee, C. F., Parravano, A., & Hollenbach, D. J. 2015, ApJ, 814, 13
- Minchev, I. & Famaey, B. 2010, ApJ, 722, 112
- Miyamoto, M. & Nagai, R. 1975, PASJ, 27, 533
- Nath, B. B., Das, P., & Oey, M. S. 2020, MNRAS, 493, 1034
- Navarro, J. F., Frenk, C. S., & White, S. D. M. 1996, ApJ, 462, 563
- Núñez-Castiñeyra, A., Nezri, E., Mollitor, P., Devriendt, J., & Teyssier, R. 2023, Journal of Cosmology and Astroparticle Physics, 2023, 012
- Patil, A. A., Bovy, J., Jaimungal, S., Frankel, N., & Leung, H. W. 2023, MNRAS, 526, 1997
- Reynolds, T. M., Fraser, M., & Gilmore, G. 2015, MNRAS, 453, 2885
- Ryden, B. & Pogge, R. 2021, Interstellar and Intergalactic Medium
- Sarbadhicary, S. K., Wagner, J., Koch, E. W., et al. 2023, arXiv e-prints, arXiv:2310.17694
- Schönrich, R. & Binney, J. 2009, MNRAS, 396, 203
- Sellwood, J. A. & Binney, J. J. 2002, MNRAS, 336, 785
- Struck, C. & Elmegreen, B. G. 2017, Monthly Notices of the Royal Astronomical Society, 469, 1157–1165
- van der Wel, A., Chang, Y.-Y., Bell, E. F., et al. 2014, ApJ, 792, L6
- Vera-Ciro, C., D’Onghia, E., Navarro, J., & Abadi, M. 2014, The Astrophysical Journal, 794, 173
- Vihola, M. 2020, In Wiley StatsRef: Statistics Reference Online
- Walter, F., Brinks, E., de Blok, W. J. G., et al. 2008, The Astronomical Journal, 136, 2563
- Watkins, E. J., Barnes, A. T., Henny, K., et al. 2023, ApJ, 944, L24
- Wu, J., Struck, C., D’Onghia, E., & Elmegreen, B. G. 2020, Monthly Notices of the Royal Astronomical Society, 499, 2672–2684
- Yadav, N., Mukherjee, D., Sharma, P., & Nath, B. B. 2017, MNRAS, 465, 1720

## Appendix A: Effect of dynamical friction on a spherical cavity propagating through a uniform medium

Consider an idealized situation, in which a spherical cavity within the ISM is propagating through a uniform ambient medium which experiences no significant direct interaction with the ISM (except via gravity). For example, such cavity may result from energy deposition from multiple supernovae exploding within a stellar cluster (i.e. a superbubble, see e.g. Yadav et al. 2017), which can inflate a quasi-spherical region with a density several orders of magnitude below the ambient ISM. The ambient medium under consideration may be associated with the DM halo of the galaxy as well as field stars unassociated with the cluster/bubble. If the relative velocity between the bubble and the ambient medium is non-zero on average (this notion will be made more precise below), the particles comprising this medium that propagate through the bubble exert a non-zero net force on the bubble (more precisely, the bubble walls) due to dynamical friction.

First, consider a single particle of mass  $m$  propagating through a spherical cavity of radius  $R$  with impact parameter  $b$ . According to Newton's shell theorem, the gravitational influence of a spherical density distribution can be reduced to the case where the mass internal to the test particle radius  $r$  from the symmetry center is concentrated into said center. The theorem is also applicable to a spherically symmetric "hole" within an otherwise uniform medium (ISM); in this case, if  $r < R$ , the effective internal mass is  $M(< r) = -4\pi r^3 \rho_{\text{ISM}}/3$ , where  $\rho_{\text{ISM}}$  is the ISM mass density, and vanishes if  $r > R$  (here we have assumed that the material evacuated from the cavity is concentrated in a narrow region near its edge and that the total mass is conserved). Hence, while the particle is at  $r > R$ , it propagates within the large-scale galactic gravitational potential as if the cavity was not present, while at  $r < R$  it experiences an effective extra contribution from the "missing" mass internal to radius  $r$ .

### A.1. Cavity of fixed radius

Let us first consider the case in which the radius of the cavity does not change appreciably over timescales of interest. If the mass of the particle entering the cavity satisfies  $m \ll M$ , then the total energy of the particle before and after the encounter remains constant in the frame of the perturber (cavity), i.e.  $\Delta v = 0$ . If the particle velocity further satisfies the condition  $v^2 \gg G\rho_{\text{ISM}}R^2$ , its trajectory is altered only slightly upon traversing the cavity (compared with the case where the bubble is absent). Hence, the change  $\Delta \vec{v}$  in particle velocity is approximately perpendicular to  $\vec{v}$  after the encounter. The perpendicular component of acceleration at  $r < R$  can be written as

$$\dot{v}_{\perp} \approx \frac{GM(< r)}{r^2} \cos \phi = \frac{4\pi G\rho_{\text{ISM}}b}{3}, \quad (\text{A.1})$$

where  $\phi$  is the angle between the pericentre and the current position of the particle (measured from the center of the cavity), and  $b$  is the impact parameter. The total change  $\Delta \vec{v}_{\perp}$  is obtained by integrating over the time interval that the test particle spends within the cavity. Writing  $dt = d(b \tan \phi / v) \approx bd\phi / \cos^2 \phi$  and observing that  $r < R$  requires  $-\sqrt{R^2 - b^2}/b < \tan \phi <$

$\sqrt{R^2 - b^2}/b$ , one obtains

$$\begin{aligned} \Delta \vec{v}_{\perp} &= \int_{\phi_{\min}}^{\phi_{\max}} \frac{4\pi G\rho_{\text{ISM}}b}{3} \frac{bd\phi}{v \cos^2 \phi} = \frac{4\pi G\rho_{\text{ISM}}b^2}{3v} \tan \phi \Big|_{-\sqrt{R^2 - b^2}/b}^{\sqrt{R^2 - b^2}/b} \\ &= \frac{8\pi G\rho_{\text{ISM}}}{3v} b \sqrt{R^2 - b^2}. \end{aligned} \quad (\text{A.2})$$

Since the scalar  $v$  remains unchanged by the encounter, the parallel component of the velocity change can be approximated as

$$\Delta v_{\parallel} = \sqrt{v^2 - v_{\perp}^2} - v \approx -\frac{v}{2} \left( \frac{\Delta v_{\perp}}{v} \right)^2 = -\frac{32\pi^2 G^2 \rho_{\text{ISM}}^2}{9v^3} b^2 (R^2 - b^2). \quad (\text{A.3})$$

The corresponding transfer of parallel momentum is  $\Delta p_{\parallel} = m\Delta v_{\parallel}$ .

The rate of momentum transfer (i.e. the effective drag force) for a collimated beam of particles of density  $n$  is obtained by multiplying (A.3) by the particle flux  $nv$  and integrating over the impact parameter, i.e.

$$\begin{aligned} F_{\parallel, \text{coll}} &= \int \Delta p_{\parallel} nv 2\pi b db = -\frac{64\pi^3 G^2 \rho_{\text{ISM}}^2}{9v^2} \rho \int_0^R b^3 (R^2 - b^2) db \\ &= -\frac{16\pi^3 G^2 \rho_{\text{ISM}}^2 \rho R^6}{27v^2}, \end{aligned} \quad (\text{A.4})$$

where  $\rho = mn$  is the mass density of incident particles and  $2\pi b db$  is a surface element perpendicular to the particle flux.

For an arbitrary distribution of particles, one should substitute

$$\rho \rightarrow m \int f(\vec{v}) d^3 v, \quad (\text{A.5})$$

where  $f(\vec{v})$  is the phase space density, to obtain

$$\vec{F} = -\frac{16\pi^3 G^2 \rho_{\text{ISM}}^2 R^6}{27} m \int \frac{f(\vec{v})}{v^2} \vec{\omega} d^3 v, \quad (\text{A.6})$$

where  $\vec{\omega} = \vec{v}/v$  is a unit vector in the direction of the incident particle velocity.

If the incident particle distribution is isotropic, then eq. (A.6) shows that the net momentum exchange vanishes, as is expected from symmetry considerations. Next, let us consider the simplest nontrivial case, in which the phase space density is isotropic in a frame that propagates with a velocity  $\vec{v}_0$  relative to the perturber (cavity). By symmetry, the dynamical friction force must be parallel to  $\vec{v}_0$ , hence we will consider only the  $\vec{F} \parallel \vec{v}_0$  component when taking the angular integral. Making use of the fact that  $f(\vec{v})$  is invariant upon Galilean transformations (or indeed Lorentz transformations if written in terms of  $\vec{p}$ ) and so is  $d^3 v$ , one obtains

$$F = -\frac{16\pi^3 G^2 \rho_{\text{ISM}}^2 R^6}{27} m \int \frac{f'(v')}{v'^2} \cos \theta d^3 v', \quad (\text{A.7})$$

where  $\vec{v}' = \vec{v} - \vec{v}_0$  is the particle velocity in the isotropy frame and  $\cos \theta = \omega \cdot \vec{v}_0 / v_0 = \vec{v} \cdot \vec{v}_0 / (v v_0)$ . Using the cosine rule to express  $\cos \theta = (v^2 + v_0^2 - v'^2) / 2v v_0$  and  $v^2 = v'^2 + v_0^2 + 2v' v_0 \cos \theta'$ , where  $\cos \theta' = \vec{v}' \cdot \vec{v}_0 / (v' v_0)$ , one can write eq. (A.7) as

$$\begin{aligned} F &= -\frac{16\pi^3 G^2 \rho_{\text{ISM}}^2 R^6}{27} m \int f'(v') v'^2 dv' \\ &\times \int \frac{1 + q \cos \theta'}{v_0^2 (1 + q^2 + 2q \cos \theta')^{3/2}} d\phi' d \cos \theta'. \end{aligned} \quad (\text{A.8})$$

Here we have expressed the velocity space element as  $d^3v' = v'^2 dv' d\phi' d\cos\theta'$ , where  $d\phi' d\cos\theta'$  is the solid angle in the isotropy frame, and defined  $q \equiv v'/v_0$ . The integral over the azimuthal angle  $\phi'$  is trivial and contributes a factor  $2\pi$ . The integral over  $\cos\theta$  is also elementary, yielding  $2/v_0^2$ , hence the final result is

$$F = -\frac{64\pi^3 G^2 \rho_{\text{ISM}}^2 R^6 m}{27v_0^2} \int f'(v') v'^2 dv'. \quad (\text{A.9})$$

## A.2. Cavity of time-dependent radius

In case of an expanding or contracting cavity the entry and exit radii of a particle traversing it will be different and the kinetic energy of the latter is no longer conserved by the encounter even if  $m \ll M$ .

In the frame of the cavity, the radial component of a particle's equation of motion within the cavity reads

$$\frac{dv_r}{dt} = \frac{d}{dt} \left( \vec{v} \cdot \frac{\vec{r}}{r} \right) = F_r + \frac{L^2}{r^3}, \quad (\text{A.10})$$

where  $L = r^2\dot{\theta}$  is the (conserved) angular momentum of the particle. Using the relation  $dv_r/dt = (1/2)dv_r^2/dr$  and writing  $F_r = -d\Phi(r)/dr$ , one obtains

$$\frac{d}{dr} \left( \frac{v_r^2}{2} + \Phi + \frac{L^2}{2r^2} \right) = 0, \quad (\text{A.11})$$

or simply  $v^2/2 + \Phi = E = \text{constant}$ , where  $E$  is the conserved total energy.

For the cavity we can write

$$\Phi(r) = -\frac{2\pi G \rho_{\text{ISM}} r^2}{3} = -\frac{1}{4} v_{\text{ch}}^2 \frac{r^2}{R_{\text{enter}}^2}, \quad (\text{A.12})$$

where  $R_{\text{enter}}$  is the entry radius and we have introduced a characteristic velocity

$$v_{\text{ch}} = \sqrt{\frac{8\pi G \rho_{\text{ISM}} R_{\text{enter}}^2}{3}}. \quad (\text{A.13})$$

Applying the energy conservation condition, one obtains the kinetic energy gain as a function of entry and exit radii into/from the bubble,

$$v_{\text{out}}^2 = v_{\text{in}}^2 + \frac{v_{\text{ch}}^2}{2} \left[ \left( \frac{R_{\text{exit}}}{R_{\text{enter}}} \right)^2 - 1 \right]. \quad (\text{A.14})$$

For a given  $R_{\text{enter}}$ , the exit radius  $R_{\text{exit}}$  can be determined by solving Eq. (A.11) for  $r(t)$  and subsequently eliminating  $t$  from  $r(t) = r_{\text{exp}}(t)$ , where  $r_{\text{exp}}(t)$  characterizes the evolution of the bubble radius. In general, the latter step has to be performed numerically. For a spherically symmetric bubble,  $R_{\text{exit}}$  is a function of entry time  $t_{\text{in}}$  (which also determines  $R_{\text{enter}} = r_{\text{exp}}(t_{\text{in}})$ ), particle velocity  $v$ , and the angle  $\theta$  between particle velocity and the local bubble surface normal at  $t_{\text{in}}$ .

### A.2.1. Integration over phase space

Once the energy/momentum gain or loss of a single particle entering the bubble at a given  $t$  and  $R_{\text{enter}} = r_b(t)$  is known, the next task is to determine the net transfer rate of a population of particles characterized by a phase space density  $f(\vec{v})$ . For this

we first need to find the number of particles crossing the bubble surface element in unit time. The inward particle flux in the frame comoving with the surface element is (defined as positive definite)

$$dF_{\text{in}} = - \left( \vec{v}^\dagger \cdot \frac{\vec{v}_{\text{exp}}}{v_{\text{exp}}} \right) f^\dagger(\vec{v}^\dagger) d^3v^\dagger, \quad (\text{A.15})$$

where  $\vec{v}^\dagger = \vec{v} - \vec{v}_{\text{exp}}$  is the particle velocity in the surface element frame,  $\vec{v}$  is its velocity in the bubble frame (i.e. its center), and  $\vec{v}_{\text{exp}}$  is the local velocity of the surface element in the same frame. The scalar product in Eq. (A.15) can be written as  $-\vec{v}^\dagger \cdot \vec{v}_{\text{exp}}/v_{\text{exp}} = -|v| \cos\theta + v_{\text{exp}} > 0$ , where  $\cos\theta$  is the angle between the particle velocity and the local radial direction in the bubble frame. Note that this quantity has to be positive, which places a constraint on the angles at which particles of given a velocity can enter the bubble. The particle flux thus becomes

$$dF_{\text{in}} = (v_{\text{exp}} - |v| \cos\theta) f(\vec{v}) d^3v, \quad \text{where} \quad \cos\theta < \frac{v_{\text{exp}}}{|v|}, \quad (\text{A.16})$$

and we have again used the invariance of  $f$  and  $d^3v$  by dropping the symbol  $\dagger$ . The normalisation of  $f$  gives the number density of stars, or physical density if multiplied with the mass of a star

$$m \int f(\vec{v}) d^3v = \rho^* \quad (\text{A.17})$$

Next, let us assume that a reference frame exists in which the particle distribution is isotropic (referred to below as the lab frame), and that the bubble propagates with a velocity  $\vec{v}_b$  relative to this frame. The total rate of momentum transfer between the bubble and the particle population can then be written as

$$\frac{dP}{dt} = \int m \Delta v_{\parallel} \cos\theta_v dF_{\text{in}} dS_b. \quad (\text{A.18})$$

Here  $m \Delta v_{\parallel}$  is the transferred momentum of a single particle parallel to its initial direction of propagation (the net transfer of transverse momentum vanishes by symmetry in a homogeneous particle field and a spherically symmetric perturber),  $\theta_v$  is the angle between the velocity  $\vec{v}$  of the incoming particle and the bubble velocity  $\vec{v}_b$  measured in the bubble frame, and  $dF_{\text{in}}$  is the particle flux defined by Eq. (A.16). The bubble surface element is

$$dS_b = R_{\text{enter}}^2 d\cos\theta d\phi, \quad (\text{A.19})$$

where the angles refer to the polar and azimuthal angles of the local surface normal vector in a coordinate system anchored to the incoming particle velocity  $\vec{v}$  (in the bubble frame). Such choice is motivated by the fact that in this coordinate system the integrand of Eq. (A.18) is independent of  $\phi$  and the corresponding integral thus immediately yields  $2\pi$ .

To make further use of the symmetries in the problem, the integral over particle velocities is best taken in the frame where the distribution is isotropic (i.e. lab frame, denoted by prime) by writing  $f(\vec{v}) d^3v = f'(\vec{v}') d^3v' = f'(v') v'^2 dv' d\cos\theta'_v d\phi'_v$ , where  $\theta'_v$  denotes the angle between  $\vec{v}'$  and  $\vec{v}_b$ . By symmetry, the integral over the corresponding azimuth  $\phi'_v$  is again trivial and gives  $2\pi$ .

To proceed further, we need the relations between particle velocities and angles in the lab and bubble frames. Defining  $\beta'_b = v_b/v'$ , one obtains

$$\cos\theta_v = \frac{\cos\theta'_v - \beta'_b}{\sqrt{1 - 2\cos\theta'_v \beta'_b + \beta'^2_b}}, \quad v = v' \sqrt{1 - 2\cos\theta'_v \beta'_b + \beta'^2_b}. \quad (\text{A.20})$$

Putting all of the above together, Eq. (A.18) takes the form

$$\begin{aligned} \frac{dP}{dt} = & 4\pi^2 m R_{\text{enter}}^2 \int_{-\infty}^{\infty} f'(v') v'^3 dv' \int_{-1}^1 (\cos \theta'_v - \beta'_b) d \cos \theta'_v \\ & \times \int_{D_\theta} (\beta - \cos \theta) \Delta v_{\parallel} d \cos \theta, \end{aligned} \quad (\text{A.21})$$

where

$$D_\theta = \{\cos \theta : \cos \theta \geq -1 \wedge \cos \theta \leq \min(1, \beta)\} \quad (\text{A.22})$$

and  $\beta \equiv v_{\text{exp}}/|v|$ .